Two-Dimensional Image Reconstruction With Spectrally-Randomized Ultrasound Signals

F. Can Meral, Mufaddal A. Jafferji, P. Jason White, and Gregory T. Clement

***Abstract*—An ultrasound imaging method using unfocused frequency-randomized transmissions and image reconstruction from data received by a single element is experimentally demonstrated. The elements of an ultrasound imaging array are randomly assigned different frequencies and driven by a multicycle sinusoidal burst. The resulting acoustic field is spectrally unique and target localization is possible based on the *a priori* knowledge of this field. A 64-element phased array driven by arbitrary waveform generators is used in the experiments. Transmission frequencies range from 2.00 to 2.64 MHz with 10 kHz resolution. One element of the array is reserved for receiving backscattered signals and an image is reconstructed from the signals received by this single element. Reconstruction is based on cross-correlation of the received data with transmitted bursts to obtain radial elliptical projections. Multiple projections are obtained from single received data, which are back-projected to obtain an image. Successful target localization is made possible through multiple frequency-randomized acquisitions. The performance of the method is measured using images of a single point target. These images are quantified and analyzed in terms of their point spread function (PSF) and SNR. Optimum imaging parameters, such as the number of acquisitions, transmit burst length, and number of possible receivers, are obtained through further analysis of SNR. Images obtained with the frequency-randomized transmission method compared well with the performance measurements of a typical B-mode acquisition. It is demonstrated that the frequency-randomized method provides images superior to B-mode images in terms of PSF. The two-point discrimination threshold is measured to be 2 mm in the lateral and azimuth directions.**

I. Introduction

In conventional pulse–echo ultrasound imaging, axial resolution is primarily determined by signal bandwidth, whereas lateral resolution is dependent upon the signal's center frequency. Because ultrasound absorption increases with frequency, achieving a clinically relevant resolution while maintaining appreciable signal strength becomes problematic for highly absorbing structures. This is particularly relevant to applications in transcranial imaging, for which frequencies must be reduced at the expense of resolution.

Manuscript received May 9, 2013; accepted August 23, 2013. Research reported in this publication was supported by award number R01EB014296 from National Institute of Biomedical Imaging and Bioengineering of the National Institutes of Health. The content is solely the responsibility of the authors and does not necessarily represent the official views of the National Institutes of Health.

F. C. Meral, M. A. Jafferji, and P. J. White are with the Department of Radiology, Brigham and Women's Hospital, Harvard Medical School, Boston, MA (e-mail: fcmeral@bwh.harvard.edu).

G. T. Clement is with the Department of Biomedical Engineering, Cleveland Clinic, Cleveland, OH.

DOI http://dx.doi.org/10.1109/TUFFC.2013.2849

Conventional B-mode ultrasound imaging employs focused transmission schemes for spatial discrimination. Similarly, delay-and-sum beamformers are used to reconstruct images from the received data [1]. Various transmission or receive beamforming configurations have been explored for improved resolution [2]–[6] or spatial coverage [7], [8]; even unfocused transmission approaches have been suggested for insonifying the entire region of interest with a single transmission (i.e., flash transmit method using unfocused transmit pulses). These transmission configurations use seemingly coherent signals across the aperture: single-frequency transmission, unified pulse shape, and programmed phase delays to appropriately focus or steer the beam. Similarly, interpretation of the received signals using a delay-and-sum beamforming technique relies on a coherent sum of signals across the aperture. Reconstructions based on such beamforming algorithms depend on the signal magnitude at the transmit frequency, or its harmonics for tissue harmonic imaging [9]. In addition to its use for receive beamforming, phase information can be used as a secondary source of information to correct for aberrations resulting from speed of sound changes in the imaging field [10], [11].

In 2007, two alternative approaches were described which were designed to make radial resolution independent of center frequency [12], [13]. In both cases, it was hypothesized that an array of simultaneously transmitted, but spatially separated, frequencies could produce a complex phase relation between different frequencies at any given point in space. If sufficiently complex, this would result in a nearly unique time-domain waveform at any given position. In [12], wedge-shaped, single-element transducers were used to produce spatially-separated frequencies, resulting from the tapered thickness of the piezoelectric element. Image reconstruction from a single point-like receiver was possible by correlating the signal with the waveforms expected at each point in space. Using this method, it was reported that target localization using ultrasound wavelengths substantially larger than the scatterer size was achieved.

In the second approach [13], elements of a linear array were randomly assigned frequencies over a given bandwidth. A single element was then used to receive the backscattered signal. Resolution of multiple scatterers could be achieved by repeating this process with different randomized transmission sets to converge on the scattering strength at a given point in space. The reconstruction algorithm described in [13] establishes a base for the current paper.

The present work provides experimental verification of a random-frequency imaging method. Experiments were performed using point targets to evaluate the performance of the method based on characteristic measurements such as point spread function (PSF) and SNR. Reconstructed images and their corresponding characteristic measurements are presented in the results section. The method is evaluated by comparing the measured PSF with theoretically calculated values of a B-mode imager. Acquisition and reconstruction parameters are further discussed for optimizing the method. Axial and lateral resolution of the method is assessed using multiple point targets. Finally the findings, advantages, and limitations of the method are discussed, along with possible future work.

II. Theory

The random-frequency imaging approach is devised to encode a region of interest (ROI) such that the phase over the frequency spectrum is a unique function of position. It is argued in [13] that such a field can be approximated using an array of continuously driven elements, each driven at a unique randomly-selected frequency. Scattering within the ROI is recorded by a single point-like receiver and the inverse kernel associated with each point in space is applied to this signal to produce an image.

The basis of the method is illustrated by considering a series of frequency-randomized point-like sources, S, located at $\mathbf{r}_\mathrm{S}$. The pressure at a receiver at $\mathbf{r}_\mathrm{R}$ caused by a frequency-independent scattering field $q(\mathbf{r}')$ is approximated by

$$p(\mathbf{r}_\mathrm{R},\omega)=\sum_{\mathrm{S,\ ROI}} g_\omega(\mathbf{r}'\mid\mathbf{r}_\mathrm{S})g_\omega(\mathbf{r}_\mathrm{R}\mid\mathbf{r}')q(\mathbf{r}')\Delta_\mathrm{S,ROI}, \quad (1)$$

where the Green's functions change as a function of the source location because of uniqueness of the transmission frequency. Applying the known inverse function corresponding to a specific point in space, $\left[\sum_\mathrm{S} g_{\omega_\mathrm{S}}(\mathbf{r}'_\mathrm{m}\mid\mathbf{r}_\mathrm{S})g_{\omega_\mathrm{S}}(\mathbf{r}_\mathrm{R}\mid\mathbf{r}'_\mathrm{m})\Delta_\mathrm{S,ROI}\right]^{-1}$, to both sides of (1) allows the scattering strength at a given point $q(\mathbf{r}'_\mathrm{m})$ to be isolated:

$$\frac{p(\mathbf{r}_\mathrm{R},\omega)}{\left[\sum_\mathrm{S} g_{\omega_\mathrm{S}}(\mathbf{r}'_\mathrm{m}\mid\mathbf{r}_\mathbf{S})g_{\omega_\mathrm{S}}(\mathbf{r}_\mathrm{R}\mid\mathbf{r}'_\mathrm{m})\Delta_\mathrm{S,ROI}\right]} = q(\mathbf{r}'_\mathrm{m})+\frac{\sum_{\mathrm{S,\ ROI}\neq\mathrm{m}} g_{\omega_\mathrm{S}}(\mathbf{r}'\mid\mathbf{r}_\mathrm{S})g_{\omega_\mathrm{S}}(\mathbf{r}_\mathrm{R}\mid\mathbf{r}')q(\mathbf{r}')\Delta_\mathrm{S,ROI}}{\left[\sum_\mathrm{S} g_{\omega_\mathrm{S}}(\mathbf{r}'_\mathrm{m}\mid\mathbf{r}_\mathrm{S})g_{\omega_\mathrm{S}}(\mathbf{r}_\mathrm{R}\mid\mathbf{r}'_\mathrm{m})\Delta_\mathrm{S,ROI}\right]}. \quad (2)$$

The method proceeds by re-randomizing the field M times and summing the results. With each successive summation, the scattering term in (2) will increase linearly, whereas the second term on the right hand side, being random over the frequency spectrum, is confined to a distribution centered about zero. Because the scattering strength has been assumed independent of frequency, its value would contribute to the point $t=0$ of the inverse Fourier transform of the equation with respect to frequency:

$$q(\mathbf{r}'_\mathrm{m})=\int\sum_\mathrm{M}\frac{p_\mathrm{M}(\mathbf{r}_\mathrm{R},\omega)}{\left[\sum_\mathrm{S} g_{\omega_\mathrm{S}}(\mathbf{r}'_\mathrm{m}\mid\mathbf{r}_\mathrm{S})g_{\omega_\mathrm{S}}(\mathbf{r}_\mathrm{R}\mid\mathbf{r}'_\mathrm{m})\Delta_\mathrm{S,ROI}\right]_\mathrm{M}}e^{-i\omega t}\mathrm{d}\omega, \quad (3)$$

where it is assumed in this idealized case that the second term in (2) approaches zero. This process is performed over the ROI to produce an image.

III. Methods

The theory would most efficiently be tested by simultaneous transmissions from an array of transducer elements, but because of limited hardware resources, the acquisition scheme was simplified into an *ex post* numerical superposition of transmissions from individual channels.

Using the center frequency and bandwidth of the transducer as constraints, a set of frequencies were randomly assigned sequentially to transducer elements in M different randomized patterns. In the simplified acquisition scheme, two waveform generators, each connected to one transducer element at a time, sequentially actuated through the set of M frequencies, leaving enough time for propagation through the ROI, receive, and data transfer with each iteration. Once M acquisitions for an element pair were done, the waveform generators were manually switched to the next element pair and a new set of M frequencies was scanned. For each of the M acquisitions, only one A-line signal was obtained by superimposing the backscattered signals originating from different transducer elements. Because of hardware limitations, the receiver could not be fully randomized; only a constant number of receivers were available in this simplified scheme. The receive element was switched between these channels at each set of M acquisitions to ensure that consecutive acquisitions were not using the same receiver. A schematic diagram of the acquisition sequence is given in Fig. 1.

A. Experimental Setup and Data Acquisition

Experiments were performed with a 64-element phased cardiac array (P4-2, ATL Ultrasound Inc., Bothell, WA) submerged in deionized water at STP. The pulse-receive frequency responses of transducer elements were measured using an electronic pulser-receiver (5072PR, Olympus, Panametrics, Waltham, MA); the averaged frequency response over all elements was calculated (Fig. 2). Two arbitrary waveform generators (33220A, Agilent Technologies Inc., Santa Clara, CA) were programmed to generate multi-cycle bursts of sinusoids at frequencies between 2 MHz and 2.64 MHz. Function generators were phase synchronized and each one was connected to one element of the transducer array at a time (1st and 33rd, 2nd and 34th elements, etc.). The backscattered signal from the

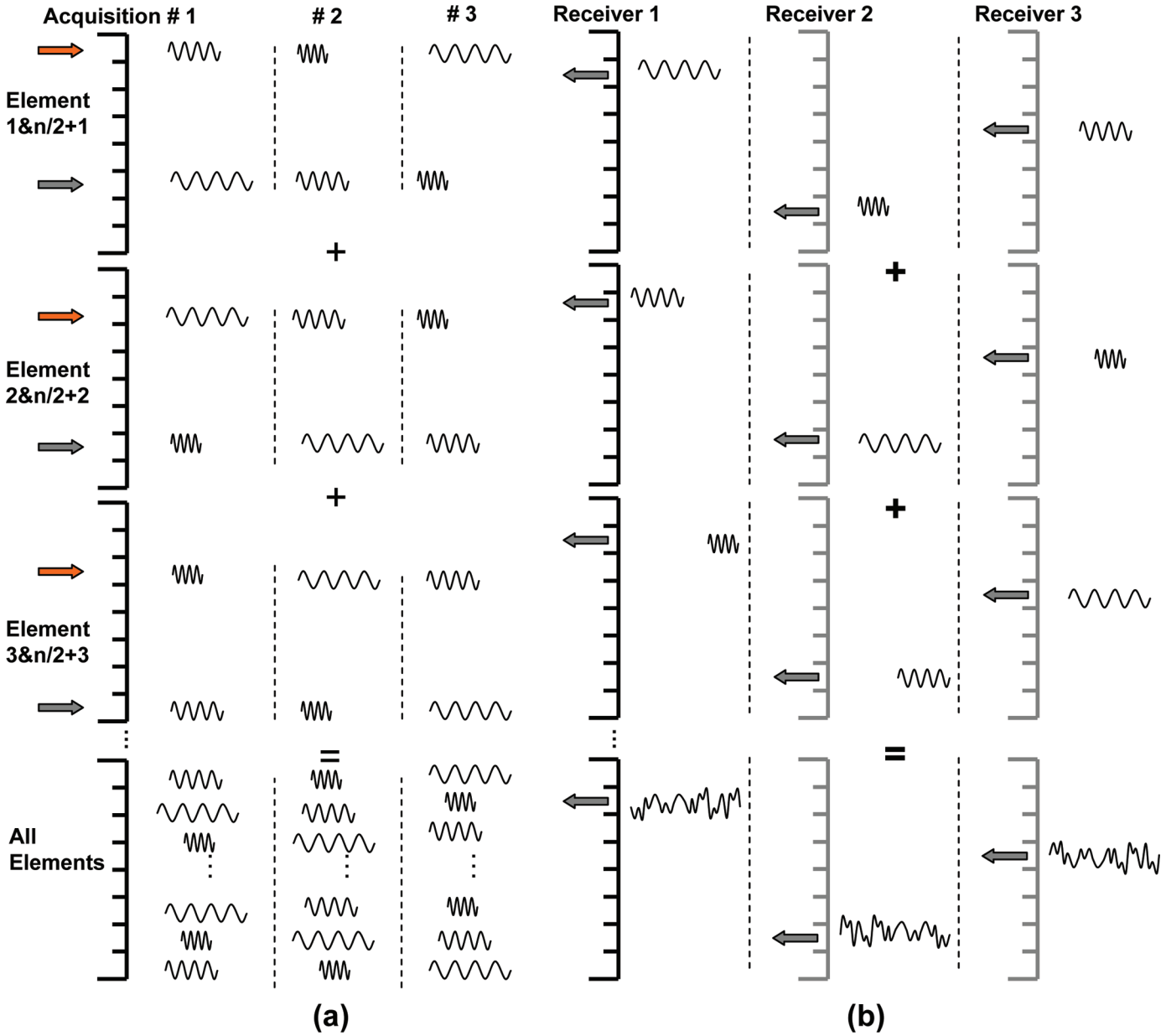

Fig. 1. A schematic illustrating the (a) transmission and (b) receive sequences used in the study. Three different acquisitions are shown in which three receivers are used. The first three rows show how each acquisition is divided into multiple pieces. The bottom row represents the original random frequency acquisition scheme that is obtained by superposition of the acquisitions above.

ROI was received by one of the three elements distributed across the aperture (elements 16, 32, or 48). Receive elements were directly connected to a four-channel oscilloscope (Tektronix Inc., Beaverton, OR), where the signal was digitized and averaged. The oscilloscope signal was sent to a personal computer and saved for further processing and image reconstruction. Data processing and image reconstruction was done with Matlab (The MathWorks Inc., Natick, MA).

B. Reconstruction Method

A pulse transmitted from a single element source located at $\mathbf{r}_{\mathrm{S}}$, $s(t)$, can be represented by its Fourier transform $S(\omega(\mathbf{r}_{\mathrm{S}}))$. An image was reconstructed for each acquisition using a single A-line signal, $p(t)$, received at $\mathbf{r}_{\mathrm{R}}$. This is similar to the expression in (1) with the addition of pulse functions $S(\omega)$,

$$p(\mathbf{r}_{\mathrm{R}},\omega) = \sum_{\mathrm{S}} S(\omega) \sum_{\mathrm{ROI}} g_{\omega}(\mathbf{r}' \mid \mathbf{r}_{\mathrm{S}}) g_{\omega}(\mathbf{r}_{\mathrm{R}} \mid \mathbf{r}') q(\mathbf{r}') \Delta_{\mathrm{ROI}} \Delta_{\mathrm{S}}. \quad (4)$$

The summation term $\sum_{\mathrm{ROI}} g_{\omega}(\mathbf{r}' \mid \mathbf{r}_{\mathrm{S}}) g_{\omega}(\mathbf{r}_{\mathrm{R}} \mid \mathbf{r}') q(\mathbf{r}') \Delta_{\mathrm{ROI}}$ is an elliptical radial projection of the scatterer field $q(\mathbf{r}')$. A solution to the scatterer field can be obtained by back-projecting the expression $p(\mathbf{r}_{\mathrm{R}},\omega)/S(\omega)$, for different source locations. Similarly, the inversion function $\sum_{S} g_{\omega_{\mathrm{S}}}(\mathbf{r}'_{\mathrm{m}} \mid \mathbf{r}_{\mathrm{S}}) g_{\omega_{\mathrm{S}}}(\mathbf{r}_{\mathrm{R}} \mid \mathbf{r}'_{\mathrm{m}}) \Delta_{\mathrm{S,ROI}}$, which was defined to reconstruct images from (1), is the projection of a point at r_{m} within the ROI. The frequency-randomized reconstruc-

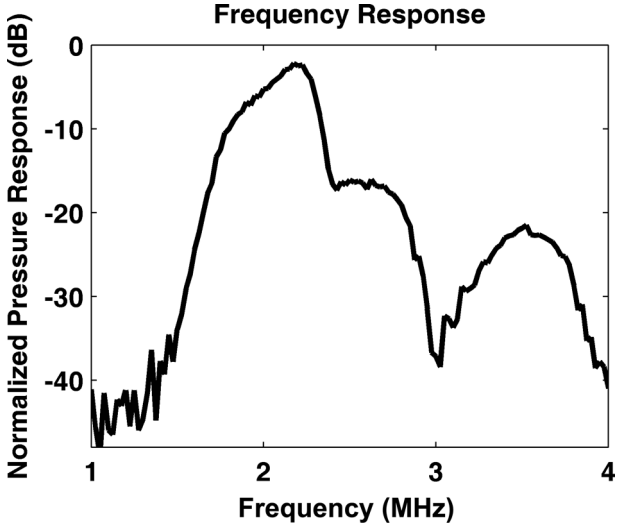

Fig. 2. Transducer pulse–receive frequency response.

tion method in [13] compares these two projections by dividing them. The quotient can be regarded as a new projection, whose inverse Fourier transform into time domain returns $q(\mathbf{r}'_{\mathrm{m}})$ at $t = 0$.

Instead of comparing two projections to obtain a pixel value, this study does a back-projection onto the entire ROI. The algorithm starts by computing the cross-correlation of the received signal, $p(\omega,\mathbf{r}_{\mathrm{R}})$, and one of the transmitted signals, $S(\omega(\mathbf{r}_{\mathrm{S}}))$. Correlation with a single pulse, $p(\omega,\mathbf{r}_{\mathrm{R}})S^{*}(\omega(\mathbf{r}_{\mathrm{S}}))$, acts like a narrowband filter, removing everything but the center frequency of transmitted pulse from the received signal. The filtered projection is obtained by inverse Fourier transform and elliptically back-projected using points r_{S} and r_{R}.

Alternatively a frequency-normalized cross-correlation: $p(\omega,\mathbf{r}_{\mathrm{R}})S^{*}(\omega(\mathbf{r}_{\mathrm{S}}))/(|p(\omega,\mathbf{r}_{\mathrm{R}})||S(\omega,\mathbf{r}_{\mathrm{S}})|)$, which returned the same phase as correlation and unity amplitude across the spectrum, can be used to obtain the filtered projection.

Even though both of these methods relied heavily on phase, the cross-correlation approach also took the amplitude of the signals into consideration; therefore, it will be called the amplitude-based reconstruction, whereas the normalized cross-correlation will be called the phase-based reconstruction. Both amplitude- and phase-based reconstruction algorithms could process the inversion problem one pulse at a time; i.e., instead of computing the inversion function for all the points in the ROI, the signal was cross-correlated with one pulse and a one-dimensional projection was obtained by inverse transforming. This was computationally less expensive than the alternative of computing the inversion functions. The inverse Fourier transform gave a peak at $t = t_{\mathrm{o}}$ in the presence of a scatterer at r. t_{o} and r are related to each other as $t_{\mathrm{o}} = c_0(|\mathbf{r}' - \mathbf{r}_{\mathrm{S}}| + |\mathbf{r}' - \mathbf{r}_{\mathrm{R}}|)$. The envelope detected radial projections, $i_{\mathrm{amp}}(r)$ or $i_{\mathrm{phs}}(r)$, depending on the correlation method utilized, were obtained by Hilbert transform and used for back-projection onto the 2-D imaging grids of the ROI. An elliptical back projection method analogous to tomography was used [14], [15]; i.e., if the pair of transmit and receive elements were coincident with the foci of an ellipse, the value of $i(r)$ corresponded to the intensity of all points on the ellipse whose major axis was r. It was further assumed that the rectangular apertures of the transducer array elements had acoustic field distributions which could be represented by sinc functions [16]. The addition of this distribution function to the back-projection improved the image by reducing the effects of side lobes. This computation, which was based on a single transmit-receive pair, was repeated for all the transmitted pulses to obtain an image from a single acquisition. Subsequent acquisitions were accumulated to obtain a final image.

Reconstructions from both methods were combined to give a single image that was superior to either image. The amplitude image acted as a weight on the phase image. A schematic diagram summarizing the reconstruction algorithm is presented in Fig. 3.

C. Point Spread Function and Signal-to-Noise Ratio

The PSF was measured using a monofilament nylon string ($d = 0.27$ mm) as a point target in the imaging plane. The effects of various acquisition parameters—such as the number of acquisitions, number of cycles in the transmitted burst, and number of receive channels used in an experiment—on the image quality were evaluated based on the PSF. The PSF consisted of a main lobe and lateral side lobes, whose intensities were compared for various parameters. The SNR was defined as the ratio of the mean image intensity of the point target within the full-width at half-maximum (FWHM) to the standard deviation of intensities outside this area. The SNR was calculated for all cases and used to optimize the parameters.

The transmit pulse length was controlled using the number of cycles within each burst, and set between 3 and 16 cycles. The setup allowed for the use of three receive channels, which was further extended to 6 and 9 receive channels by combining data from the series of experiments with different receivers (elements 8, 40, and 57 for 6 receive channels; elements 24, 33, and 60 for 9 receive channels). Data from these series of experiments was reorganized to obtain artificial data sets of experiments mimicking different numbers of receivers, from 1 to 9. This provided the ability to measure SNR as a function of the number of acquisitions as well as the number of receivers.

D. Comparison With B-Mode

The same array geometric and mechanical properties were used to computationally estimate the axial and lateral resolution of an ideal B-mode image. These estimations were compared with the experimental results of random frequency acquisition. The lateral resolution was estimated based on the beamwidth of a geometric focus at the point target depth. Axial resolution was based on the temporal pulse width at the transducer center frequency, which was measured to be 1.21 μs, corresponding to 1.8 mm.

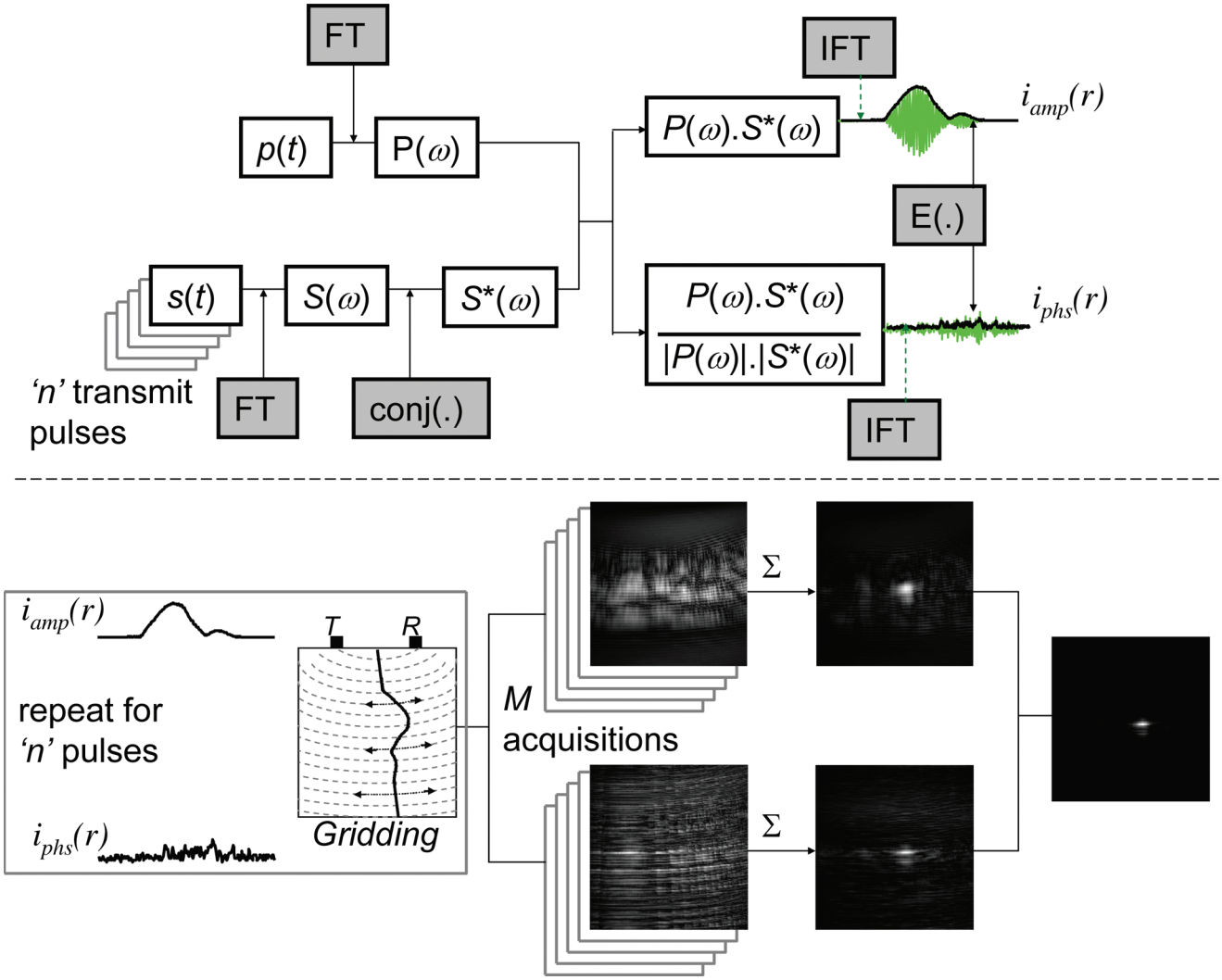

Fig. 3. Schematic diagram of the reconstruction. FT = Fourier transform; IFT = inverse Fourier transform; conj(.) = complex conjugate; E(.) = envelope detection.

E. Axial and Lateral Resolution Assessment With Multiple Targets

Two nylon strings were positioned at various distances (1, 2, and 4 mm) in the axial and lateral directions. The ability to localize multiple targets close to each other was evaluated using this setup. Three receive channels were used with 32 random acquisitions.

IV. Results

A. Transducer Array and Data Acquisition

The frequency response of the transducer array is given in Fig. 2. According to these initial results, the transducer elements had an average central frequency of 2.2 MHz and an average −6-dB fractional bandwidth of 22%. To transmit at 64 different frequencies, an extended bandwidth of 29% was used. Corresponding transmit frequencies were between 2 MHz and 2.63 MHz with 10 kHz steps.

B. Image Reconstruction Method

In all images, the transducer array is located at the top, with the axis of forward propagation oriented downward. The origin of rectangular coordinate system is located on the transducer array at its leftmost point. The images were reconstructed using the amplitude- and phase-based reconstruction algorithms from a single random frequency acquisition ($M = 1$); these are given in Fig. 4, together with a combined image. The SNRs in these figures are very low and successful localization of the point target was not possible. However, accumulation through reconstruction of successive random sets demonstrates significant improvement. Images reconstructed from multiple random sets ($M = 48$) with both reconstruction approaches are presented in Fig. 5; a combined image is also given. The first two images demonstrate the successful localization of the point target with sufficient SNR and the combined image has substantially higher SNR (34.7 versus 14.4 or 15.1).

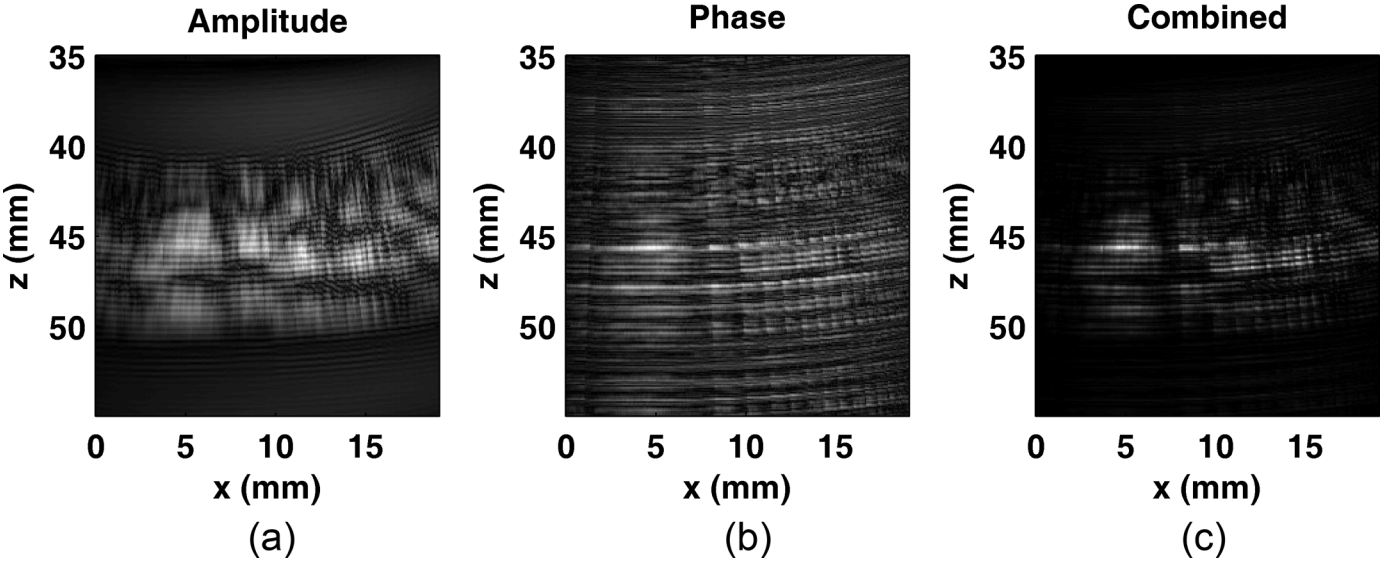

Fig. 4. Reconstructed random-frequency image of a point target, single acquisition ($M = 1$). (a) Amplitude-based (SNR = 5.1) and (b) phase-based reconstruction (SNR = 5.0). (c) Amplitude- and phase-based images combined; the combined image fails to localize the point target at its correct position.

C. Point Spread Function and Signal-to-Noise Ratio

The data from Fig. 5 were used as PSFs to measure the FWHM in the axial and lateral directions. The amplitude-based image yielded an axial FWHM of 1.58 mm and a lateral FWHM of 1.88 mm. The phase-based image yielded an axial FWHM of 0.53 mm and a lateral FWHM of 2.28 mm. The combined image yielded an axial FWHM of 0.45 mm and a lateral FWHM of 1.35 mm. The SNR was 14.4 for the amplitude image, 15.1 for the phase image, and 34.7 for the combined image. These measurements of FWHM, PSF, and SNR provide comparisons between two reconstruction algorithms and demonstrate how the combination image presents substantial improvement. Hereafter, amplitude- and phase-based methods will no longer be separated and only the combined method will be considered for analyses.

The effect on image quality of various acquisition parameters, such as the number of transmitted cycles or the number of receivers, was evaluated based on PSF measurements and side lobe sizes. The side lobes mentioned here are not related to the radiation pattern of the acoustic source; they are actually imaging artifacts that are observed on two sides of the target point location. Within this context, these lateral artifacts are called side lobes; also the target point is called the main lobe. Fig. 6 displays four images acquired with different parameters, as well as vertical and horizontal section cuts from these im-

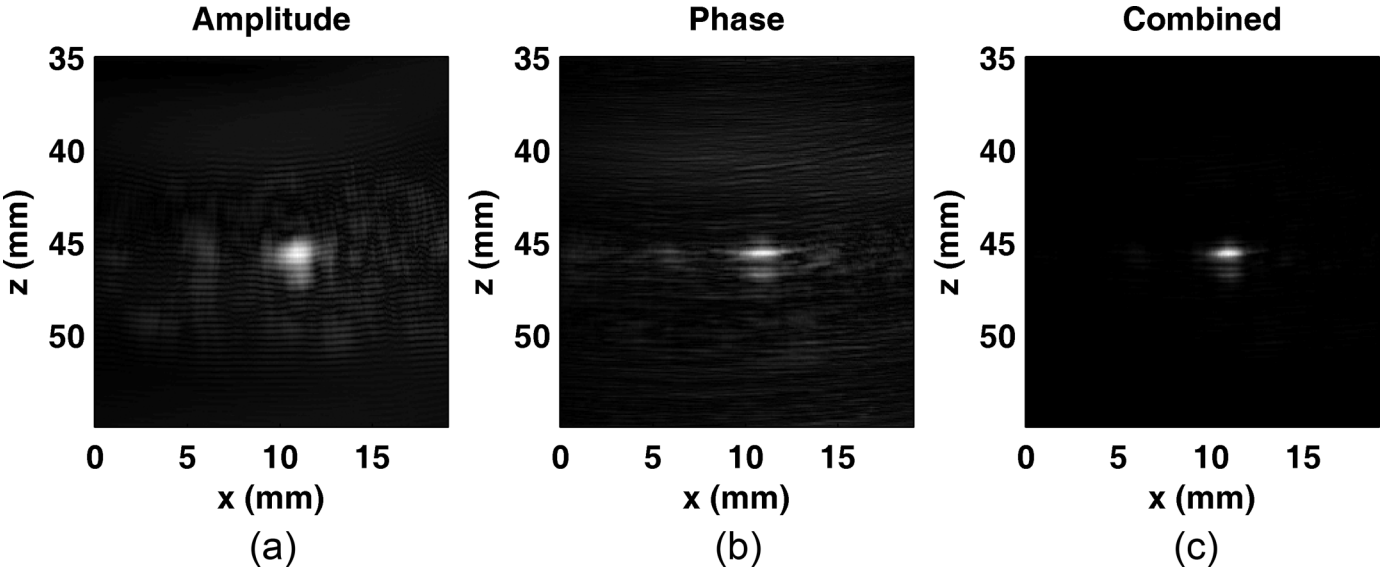

Fig. 5. Reconstructed random-frequency image of a point target, multiple acquisitions ($M = 48$). (a) Amplitude-based (SNR = 14.4) and (b) phase-based reconstruction (SNR = 15.1). (c) Amplitude- and phase-based images combined (SNR = 34.7).

ages. The first image, Fig. 6(a), is a benchmark image acquired with 3 receivers and a 16-cycle transmit burst. The SNR for this image is 29.7 and side-lobes are at 14.3% of the main lobe. The second image, Fig. 6(b), uses 3-cycle transmit pulses. The dramatic increase in the side-lobes, up to 48.3%, and therefore reduction in the image quality, SNR down to 18.5, can be observed, resulting from the reduction in the number of cycles in the burst length from 16 to 3 cycles. Figs. 6(c) and 6(d) were reconstructed using a series of experiments to mimic 6 or 9 receiver channels, and both display slightly better images compared with the benchmark image; the SNR is 31.9 for the 6-receiver case and 36.1 for the 9-receiver case. Both of these images present reduced lateral side-lobes, 8.9% and 4.0% respectively, which can be observed in Fig. 6(f). The main lobe has a lateral width of 1.36 mm for the benchmark image and it was unaffected by a change in the number of receivers. However, for the 3-cycle transmit burst case, the main lobe widened to 1.95 mm. The axial width of the PSF main lobe was 0.68 mm, which was equal to a wavelength, for the first two images with 3 receivers, and drops down to 0.45 for the 6- and 9-receiver images.

The SNR was measured as a function of number of acquisitions for these four cases; results are presented in Fig. 7. It can be observed from the figure that with increasing number of acquisitions, the SNR asymptotically approached a constant for each case. The SNR reaches a constant value with lower number of acquisitions when there are fewer receiver channels at the expense of lowered SNR. Conversely, a higher SNR was obtained when more receivers were used; however, more acquisitions were required before the SNR reached a final value. The number of acquisitions versus SNR behavior can be approximated by an exponential curve: $A(1 - \exp(-\nu m))$, where A is the SNR convergence value, m is the number of acquisitions, and ν is an exponential constant denoting the convergence speed.

Parameters A and ν, characterizing the SNR curves, are further analyzed as functions of the number of receive channels as well as the number of acquisitions. Artificially organized data sets from three different experiments that were used to mimic different cases with from 1 to 9 receivers were analyzed based on the parametric curves. Images reconstructed from these data sets and their SNR were calculated for every m. SNR-versus-m plots were obtained and fitted with exponential curves. Results for the best-fit parameters are presented in Fig. 8.

As can be seen from Fig. 8, increasing the number of receivers increases the measured SNR. However, Fig. 8 indicates that reaching this SNR required an increased number of acquisitions. Even though the receive channels for this analysis were not selected randomly— rather, they

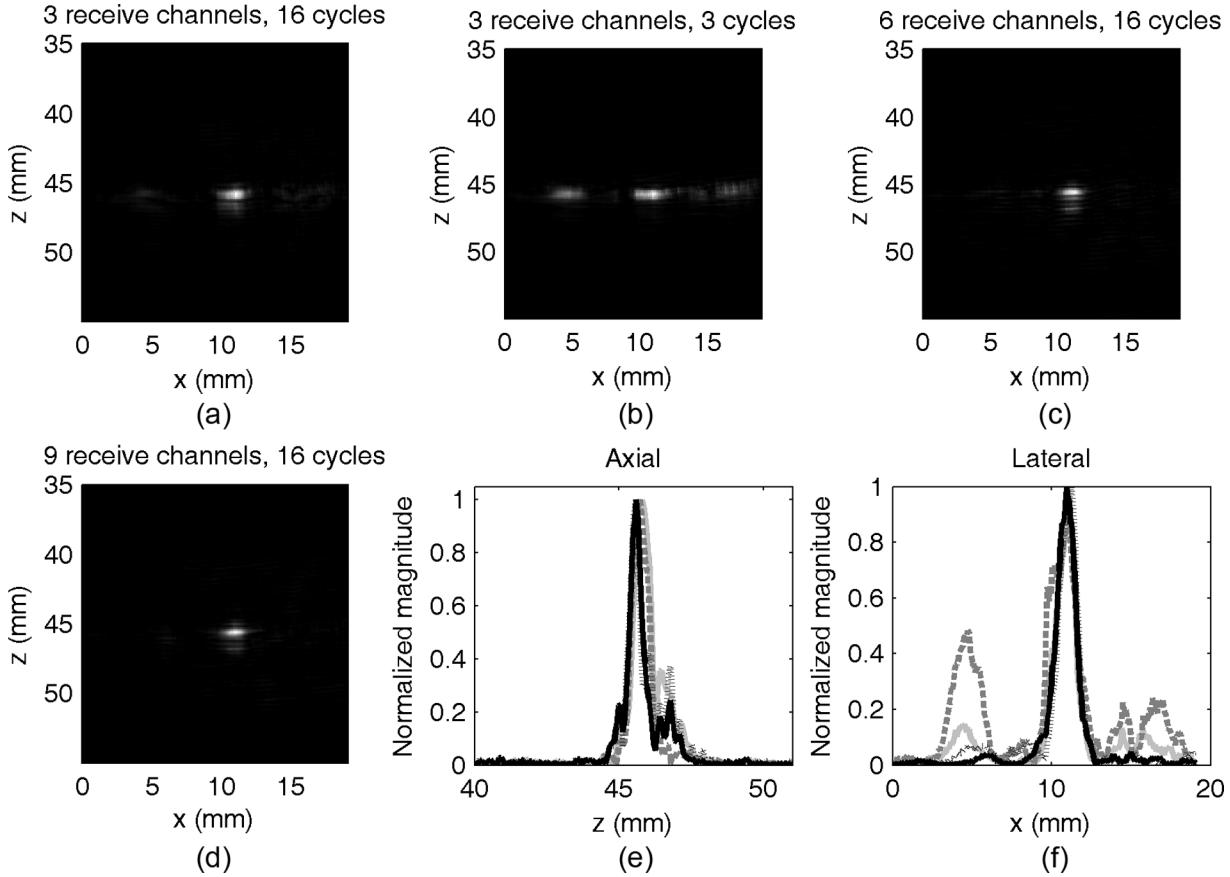

Fig. 6. Images correspond to different acquisition parameters: (a) 3 receive channels, 16-cycle transmit burst, dashed line in (e) and (f); (b) 3 receive channels, 3-cycle transmit burst, solid gray line; (c) 6 receive channels, 16-cycle transmit burst, dotted line; (d) 9 receive channels, 16-cycle transmit burst, solid black line. PSF section cuts in (e) axial and (f) lateral directions.

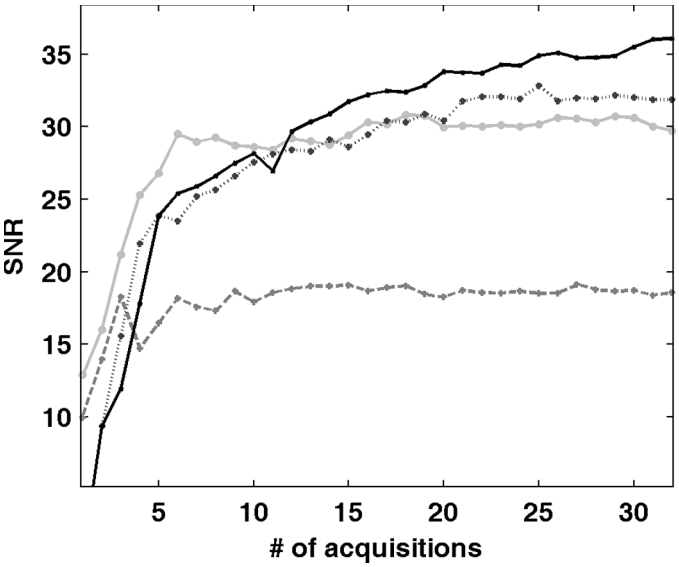

Fig. 7. SNR as a function of number of acquisitions. Solid gray line: 3 receive channels, 16-cycle transmit burst; dashed line: 3 receive channels, 3-cycle transmit burst; dotted line: 6 receive channels, 16-cycle transmit burst; solid black: 9 receive channels, 16-cycle transmit burst.

were handpicked to create an equally spaced distribution of receivers across the aperture—the figure shows the convergence behavior of SNR as a function of the number of receivers.

D. Axial and Lateral Resolution Assessment With Multiple Targets

Acquisitions with multiple targets aligned vertically or horizontally were reconstructed to assess the method's ability to localize multiple targets. Images are given in Fig. 9.

Even though the PSF had a measured axial FWHM of 0.68 mm, in the presence of multiple targets aligned vertically with 1 mm between them, the method performs poorly, and cannot localize both targets. As the distance between two targets was increased to 2 mm and 4 mm, both target points became resolvable in the image. This is summarized in the vertical-section cuts shown in Fig. 9(d). Similar findings were observed when the points were aligned horizontally. This time, however, it was predicted that objects closer than 1 mm to each other would not be resolved based on the lateral FWHM of the PSF, which was 1.35 mm. Multiple points could be successfully localized when they were 2 mm or 4 mm apart. Another noted difference is about the resulting intensities; even though both targets were identical, they appeared in the image with different intensities.

V. Discussion

A method similar to the one which was previously described as two-dimensional image reconstruction with unfocused randomized signals [13] is demonstrated using a low-frequency clinical transducer array and basic data acquisition hardware. This method relies heavily on the unique phase field crated by randomly assigned transducer frequencies. A backscattered signal can be processed to reconstruct a two-dimensional image based on its phase if the random phase field is known. In the earlier study, the random-frequency methodology was simulated using a hypothetical ultrasound transducer array of 202 elements and 1.15 MHz bandwidth centered at 675 kHz. An array with these specifications was not readily available; however, to provide proof of concept of the method. For the experiments, a clinical array from the low end of the frequency spectrum was chosen to obtain a high fractional bandwidth. Pulse–echo frequency response of the transducer array shows some degradation; therefore, a limited range of frequencies was used in the experiments. The selected frequency range still shows a variation greater than 10 dB. Despite these less-than-ideal conditions for the transducer array, the random-frequency method was successfully implemented and demonstrated.

The reconstruction algorithm presented in this research is slightly different from the original algorithm proposed for random-frequency imaging; however, it provides a close approximation to the solution. Of the two approaches presented, the amplitude-based reconstruction provides better lateral and amplitude resolution, whereas the phase-based reconstruction has superior axial resolution. Using the amplitude of the former approach to window the reconstruction obtained by the latter approach results in images superior to either method, which was demonstrated through PSF analysis and justifies the combination of the two methods.

PSF measurements can be compared with the theoretical calculations of ideal B-mode performance of the same array. Such an array can geometrically focus to cre-

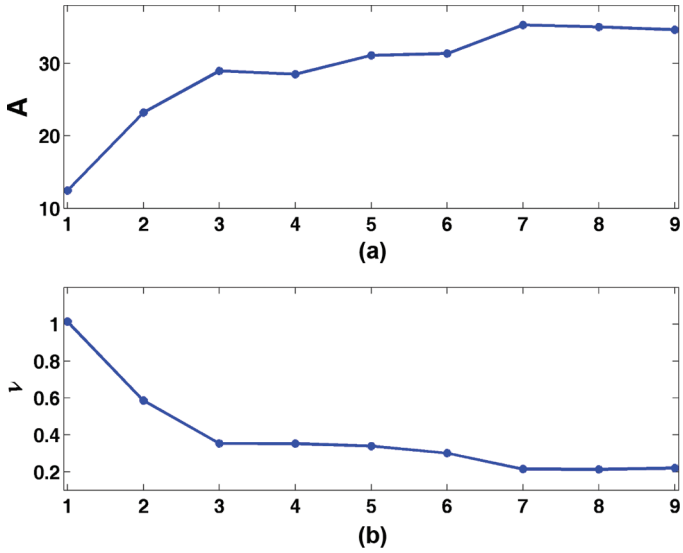

Fig. 8. Curve fit parameters for the SNR versus number of acquisitions. (a) A is the highest possible SNR that can be obtained with the current set of receivers; (b) ν is the convergence speed to the highest possible SNR.

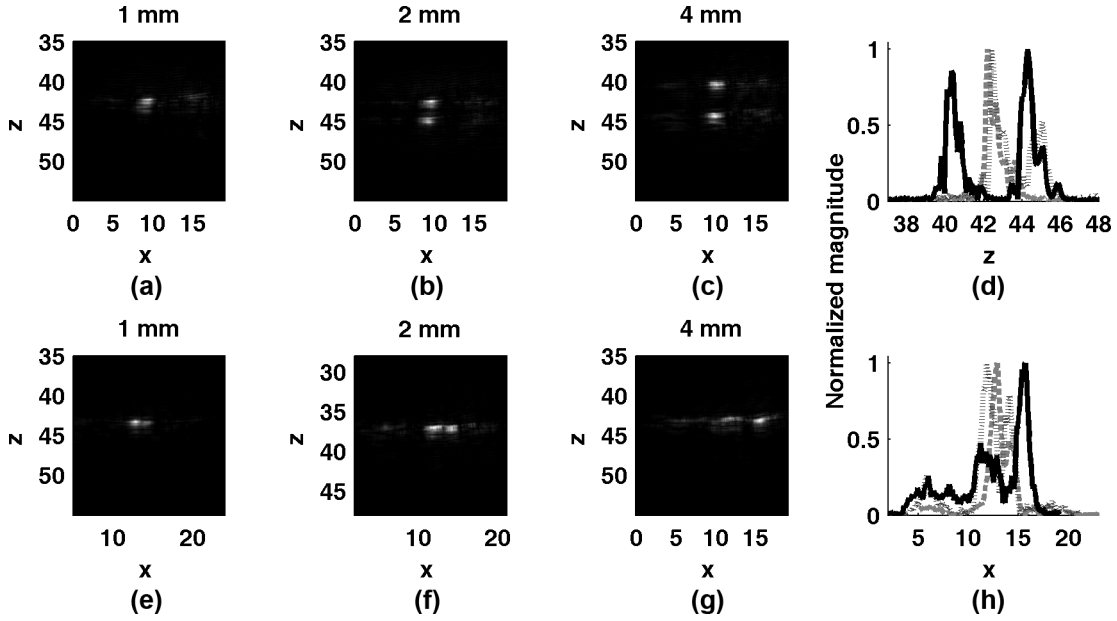

Fig. 9. Two point targets positioned vertically (a) 1 mm, (b) 2 mm, and (c) 4 mm apart, and horizontally (e) 1 mm, (f) 2 mm, and (g) 4 mm apart. (d) Vertical section cut through point targets, and (h) horizontal section cut through point targets. Dashed line: 1 mm, dotted line: 2 mm, and solid line: 4 mm separation. All dimensions are in millimeters.

ate a beam with a lateral FWHM of 1.36 mm. This is almost equal to 1.35 mm (error less than 1%), which is demonstrated through PSF analysis of this study as its lateral resolution limit. Similarly, the best axial resolution obtained was presented as 0.45 mm, which is again superior to the axial resolution that can be obtained using a B-mode imager, which is the temporal pulse width at the transducer's central frequency, and measured to be 1.8 mm for the array used. However, the performance of the random-frequency method is still to be experimentally determined for diffuse scatterers (speckle targets) and medical and biological applications, where the field is complex compared with the point targets studied in this paper.

The potential advantages provided by the random-frequency method are not limited by the image resolution. The hardware and acquisition sequence of random-frequency imaging method is much simpler than ultrasound scanners that use transmit-and-receive beamformers to create B-mode images. Although hardware beamformers are very efficient in term of computation, the method demonstrated here eliminates this stage altogether, reducing the necessary hardware components significantly. A typical B-mode image is created with the current transducer array using 64 focused transmit elements and 64 receive elements. This requires more hardware resources than the acquisitions demonstrated here for random frequency with optimum M ($M = 32$), which uses 32 random transmissions from all elements and 32 A-line signals received from single elements. Additionally, there is no time concern because the acquisition of 32 A-line signals requires half the time required for 64 beamformed B-mode acquisitions.

Another counterintuitive fact is the ability to improve spatial resolution by using longer transmit bursts instead of a time-localized pulse. Originally, it was proposed that continuous wave (CW) be used for transmission, however because of the hardware used in the study, this was replaced by a longer burst at a specific frequency. Maximum transmit amplitude is obtained at a minimum of 3-cycle transmit; therefore, 3 is the minimum number of cycles used for transmission. Alternatively, pulses consisting of more than 16 cycles are so long that they overlap the acquisition time window and saturate the receivers, preventing the recording of backscattered signals from the ROI. Comparison from the two extreme cases of transmission burst lengths concludes that the longest possible burst length is advantageous over shorter bursts.

One of the main shortcomings of the presented study was the limited number of receive channels; instead of access to all 64 channels, only 3 were used for the experiments. However, the parametric analysis of the SNR from a series of 3 experiments with different receivers shows little SNR improvement with the addition of these receive channels. For instance, going from 3 receive channels to 6 means doubling the receive hardware or acquisition time. This increase of channels provides only a 15% increase in the highest obtainable SNR. Similarly, increasing the number to 9 receive channels improves the highest SNR by 24%. This improved SNR comes at the expense of increasing the number of acquisitions, and thus reducing imaging speed. Fig. 8 verifies that the current setup, despite the limited number of receivers, provides sufficient acquisition flexibility for optimum SNR. It is validated through this analysis that simplifying the random-frequency acquisition into 3 receive channels does not result in a drastic reduction of the image quality. One interesting fact about the SNR is that it approaches an asymptotic limit as the number of acquisitions increases. This is due to the lim-

ited bandwidth, variation of response within this limited range, and number of elements on the array. The strength of the method comes from the uniqueness of the sound field at each acquisition; however this was not satisfied because of the limitations mentioned earlier.

The resolution limitation of the random frequency method with the current setup is evaluated using multiple targets in the axial and lateral dimensions. Findings confirm the results of PSF analysis in lateral resolution, and demonstrate that the PSF overestimates the axial resolution performance. An interesting addition from these multiple target images is the difference of intensities of two identical targets. This kind of deconstructive interference is an issue when the points are aligned horizontally, but not vertically; therefore, is believed to be a product of the poor lateral resolution of the system.

The theory suggests that the random-frequency imaging method is sensitive to the changes in speed of sound and density; therefore, it can be used to reconstruct separate maps of sound speed and density of the medium. This would be a significant contribution to medical ultrasound and requires some modifications of the reconstruction algorithm to be implemented, leaving much work to be still performed.

Obtaining high image resolution using a low-frequency broadband transducer array can be suitable for applications in which frequency-dependent absorption and phase aberrations present a challenge; for example, lowering the transducer frequency to penetrate the human skull results in a significant loss in B-mode image resolution. Random frequency imaging may present a solution to this challenging problem by achieving improved resolution while keeping the transmitted frequencies low enough for transcranial penetration, minimized absorption, and reduced phase aberrations.

Finally, the method presented here does not require any advanced circuitry, which could be a significant barrier as the number of transducer elements increases, such as two-dimensional matrix transducers for three-dimensional ultrasound imaging. Therefore, random frequency imaging presents new opportunities to be used in three-dimensional ultrasound imaging.

VI. Conclusions

This study demonstrates experimental verification of the random-frequency imaging method using a clinical transducer array. The method is effective in imaging point targets smaller than the wavelength, with axial and lateral PSF dimensions of 0.45 and 1.35 mm, respectively. These results indicate that improved imaging performance in the axial direction and comparable performance in lateral direction compared with B-mode images can be obtained while using fewer hardware resources. A broadband transducer array is essential in creating unique phase fields resulting from randomized transmissions; therefore, future experimental work should investigate the performance of a dedicated random-frequency transducer. Additionally, all of the presented work, both simulation and experimentation, is based on frequency-independent point targets. Investigating the performance of the method on homogenous scatterer fields, where scattering is a function of frequency, is essential for this method to be presented as a clinical tool.

References

[1] K. E. Thomenius, "Evolution of ultrasound beamformers," in *Proc. IEEE Ultrasonics Symp.*, 1996, vol. 2, pp. 1615–1622.
[2] M. Karaman, P. C. Li, and M. O'Donnell, "Synthetic aperture imaging for small scale systems," *IEEE Trans. Ultrason. Ferroelectr. Freq. Control*, vol. 42, no. 3, pp. 429–442, 1995.
[3] G. Cincotti, G. Cardone, P. Gori, and M. Pappalardo, "Efficient transmit beamforming in pulse-echo ultrasonic imaging," *IEEE Trans. Ultrason. Ferroelectr. Freq. Control*, vol. 46, no. 6, pp. 1450–1458, Nov. 1999.
[4] J. Capon, "High-resolution frequency-wavenumber spectrum analysis," *Proc. IEEE*, vol. 57, no. 8, pp. 1408–1418, Aug. 1969.
[5] P. Stoica, Z. Wang, and J. Li, "Robust Capon beamforming," *IEEE Signal Process. Lett.*, vol. 10, no. 6, pp. 172–175, Jun. 2003.
[6] J.-F. Synnevag, A. Austeng, and S. Holm, "Adaptive beamforming applied to medical ultrasound imaging," *IEEE Trans. Ultrason. Ferroelectr. Freq. Control*, vol. 54, no. 8, pp. 1606–1613, Aug. 2007.
[7] D. P. Shattuck, "Explososcan: A parallel processing technique for high speed ultrasound imaging with linear phased arrays," *J. Acoust. Soc. Am.*, vol. 75, no. 4, pp. 1273–1282, 1984.
[8] B. Madore, P. J. White, K. Thomenius, and G. T. Clement, "Accelerated focused ultrasound imaging," *IEEE Trans. Ultrason. Ferroelectr. Freq. Control*, vol. 56, no. 12, pp. 2612–2623, Dec. 2009.
[9] M. A. Averkiou, "Tissue harmonic imaging," in *Ultrasonics Symposium, 2000 IEEE*, 2000, vol. 2, pp. 1563–1572.
[10] S. W. Flax and M. O'Donnell, "Phase-aberration correction using signals from point reflectors and diffuse scatterers: Basic principles," *IEEE Trans. Ultrason. Ferroelectr. Freq. Control*, vol. 35, no. 6, pp. 758–767, 1988.
[11] M. O'Donnell and S. W. Flax, "Phase-aberration correction using signals from point reflectors and diffuse scatterers: Measurements," *IEEE Trans. Ultrason. Ferroelectr. Freq. Control*, vol. 35, no. 6, pp. 768–774, 1988.
[12] P. White and G. Clement, "Two-dimensional localization with a single diffuse ultrasound field excitation," *IEEE Trans. Ultrason. Ferroelectr. Freq. Control*, vol. 54, no. 11, pp. 2309–2317, Nov. 2007.
[13] G. T. Clement, "Two-dimensional ultrasound detection with unfocused frequency-randomized signals," *J. Acoust. Soc. Am.*, vol. 121, no. 1, pp. 636–647, 2007.
[14] A. C. Kak and M. Slaney, "Tomographic imaging with diffracting sources," in *Principles of Computerized Tomographic Imaging*, Piscataway, NJ: IEEE Press, 1988, pp. 203–273.
[15] S. J. Norton and M. Linzer, "Ultrasonic reflectivity tomography: Reconstruction with circular transducer arrays," *Ultrason. Imaging*, vol. 1, no. 2, pp. 154–184, Apr. 1979.
[16] R. S. C. Cobbold, *Foundations of Biomedical Ultrasound*. New York, NY: Oxford University Press US, 2007.

Authors' photographs and biographies were unavailable at time of publication.